Single-well seismic modeling in viscoelastic media using a variable-grid finite-difference method

Chunling Wu, Jerry M. Harris, and Jonathan Franklin, Stanford University*

Summary

Single-well seismic imaging has recently emerged as a valuable tool for delineating well-parallel features within structurally complex regions. Forward modeling can provide crucial guidance in both the design of single-well experiments and in the later phases of processing and data interpretation. A significant difficulty in modeling single-well data is the large range of spatial scales present: efficient inclusion of a small borehole (10-20cm) within a larger domain modeling (200-300m) requires special computational techniques.

We present a variable-grid finite-difference scheme for solving the viscoelastic wave equation in two dimensions which accommodates multiple scale features: by smoothly refining the computational mesh in the vicinity of the borehole, our method allows inclusion of a realistic well and captures the resulting propagation phenomenon including tube waves. We demonstrate the numerical efficacy of our technique on two single-well modeling problems which include both boreholes of reasonable dimensions and reflecting salt structures in the far-field. Although strong tube waves obscure some temporal regions of the data, reflections from the salt flank are evident.

Introduction

Single-well imaging techniques involve placing both a seismic source and a hydrophone string within the same well: geometries of this type allow characterization of reflectors near the borehole including high-angle faults, salt flanks (Cameron and Chen, 1995), and fracture regions (Majer et al., 1997). For structural features with near-vertical dips, single-well configurations provide favorable seismic illumination conditions in comparison to surface surveys. When horizontal boreholes exist within reservoirs, single-well measurements can aid interpreters in distinguishing local bed boundaries and fluid contacts.

Full-waveform forward modeling is an excellent tool for exploring the impacts of survey geometry and subsurface structure on imaging experiments. In the case of single-well seismic surveys, intelligent choice of acquisition parameters, such as source/receiver offset, are important in minimizing the amount of primary signal obscured by high-amplitude borehole modes. The realistic synthetic seismograms generated by forward modeling can also be used to evaluate data processing and inversion algorithms in situations where a known model is required.

Explicit finite-difference methods (FD) have historically dominated elastic wavefield modeling in geophysics because of their flexibility in representing complex models and their computational efficiency. For our application, Robertsson's velocity-stress formulation of the viscoelastic wave equation (Robertsson et al., 1994) provides a good mixture of physical realism and computational simplicity. Inclusion of attenuation in the wave propagation model allows prediction of the impact of low-Q regions on imaging. Tube wave suppression devices such as gas bubble injection can be modeled as regions of high attenuation along the borehole. Gas chimneys, poorly consolidated sediments, and other geological sources of signal attenuation are also easy to include.

Many of the strongest signals observed in borehole experiments are modes traveling within the borehole: these tube waves are often sufficient to cloak the lower amplitude reflection from an exterior target. Tube waves also reflect at changes in borehole diameter and re-radiate energy into the formation, producing multiple secondary sources. A basic requirement for accurate single-well and cross-well modeling is inclusion of these waves.

To resolve the borehole, a structural feature with tiny lateral dimensions, a very fine mesh is required (2 cm). At the same time the target of the single-well survey may be a salt flank as much as 60 m from the well with significant vertical extent. An equi-spaced mesh with sufficient resolution to describe the borehole and sufficient size to include far-field reflectors requires too much memory for simulation on most computers. Variable grid finite-difference techniques (Moczo, 1989; Jastram and Behle, 1991) provide an efficient solution to the multi-scale borehole problem (Falk et al., 1996): smooth refinement in the vicinity of the borehole allows effective representation of the well without exhausting available memory resources.

We use the fourth-order non-uniform grid FD scheme proposed by Pitarka (1999) for solution of the 2D viscoelastic wave equation in our single-well experiments. Weights for the stretched-grid operators are pre-computed using the method of undetermined coefficients, although equivalent weights can be computed using analytic differentiation of Lagrange polynomials. By smoothly varying the cell spacings from the coarse far-field mesh to the borehole domain, we avoid spurious reflections generated by the grid transition. The sections that follow present the technique in greater detail and demonstrate the method's efficacy on several single-well models.

Mathematical formulation

Following Robertsson (Robertsson et al., 1994), the 2D velocity-stress formulation for isotropic viscoelastic wave propagation with a single relaxation mechanism can be

Downloaded 01 Dec 2011 to 171.64.173.107. Redistribution subject to SEG license or copyright; see Terms of Use at http://segdl.org/

written as

$$\begin{cases} \rho\dfrac{\partial v_x}{\partial t} = \dfrac{\partial \sigma_{xx}}{\partial x} + \dfrac{\partial \tau_{xz}}{\partial z} \\ \rho\dfrac{\partial v_z}{\partial t} = \dfrac{\partial \sigma_{xz}}{\partial x} + \dfrac{\partial \sigma_{zz}}{\partial z} \\ \dfrac{\partial \sigma_{xx}}{\partial t} = \pi\dfrac{\tau_\epsilon^p}{\tau_\sigma}(\dfrac{\partial v_x}{\partial x} + \dfrac{\partial v_z}{\partial z}) - 2\mu\dfrac{\tau_\epsilon^s}{\tau_\sigma}\dfrac{\partial v_z}{\partial z} + r_{xx} \\ \dfrac{\partial \sigma_{zz}}{\partial t} = \pi\dfrac{\tau_\epsilon^p}{\tau_\sigma}(\dfrac{\partial v_x}{\partial x} + \dfrac{\partial v_z}{\partial z}) - 2\mu\dfrac{\tau_\epsilon^s}{\tau_\sigma}\dfrac{\partial v_x}{\partial x} + r_{zz} \\ \dfrac{\partial \sigma_{xz}}{\partial t} = \mu\dfrac{\tau_\epsilon^s}{\tau_\sigma}(\dfrac{\partial v_x}{\partial z} + \dfrac{\partial v_z}{\partial x}) + r_{xz} \\ \dfrac{\partial r_{xx}}{\partial t} = -\dfrac{1}{\tau_\sigma}[r_{xx} + \pi(\dfrac{\tau_\epsilon^p}{\tau_\sigma} - 1)(\dfrac{\partial v_x}{\partial x} + \dfrac{\partial v_z}{\partial z}) \\ \qquad -2\mu(\dfrac{\tau_\epsilon^s}{\tau_\sigma} - 1)\dfrac{\partial v_z}{\partial z}] \\ \dfrac{\partial r_{zz}}{\partial t} = -\dfrac{1}{\tau_\sigma}[r_{zz} + \pi(\dfrac{\tau_\epsilon^p}{\tau_\sigma} - 1)(\dfrac{\partial v_x}{\partial x} + \dfrac{\partial v_z}{\partial z}) \\ \qquad -2\mu(\dfrac{\tau_\epsilon^s}{\tau_\sigma} - 1)\dfrac{\partial v_x}{\partial x}] \\ \dfrac{\partial r_{xz}}{\partial t} = -\dfrac{1}{\tau_\sigma}[r_{xz} + \pi(\dfrac{\tau_\epsilon^s}{\tau_\sigma} - 1)(\dfrac{\partial v_x}{\partial z} + \dfrac{\partial v_z}{\partial x}), \end{cases} \tag{1}$$

where ρ is the density; π denotes the relaxation modulus for P-waves ($\pi = \lambda + 2\mu$); μ is the relaxation modulus for S-waves, equivalent to the shear modulus; and λ is the second Lame parameter. Likewise, τ_ϵ^p and τ_ϵ^s are the strain relaxation times for P- and S-waves, respectively, and τ_σ is the stress relaxation time. The particle velocity components are v_x and v_z and the stress components are σ_{xx}, σ_{zz} and σ_{xz}. The memory variables, used to approximate the time convolution in the viscoelastic wave equation (Robertsson et al., 1994), are r_{xx}, r_{zz} and r_{xz}.

If we define ω as $2\pi f$, where f is the central frequency, and introduce P- and S-wave quality factors (Q_p and Q_s) the expressions for the relaxation times can be easily written (Hestholm and Ruud, 2000):

$$\begin{cases} \tau_\sigma = \dfrac{1}{\omega}(\sqrt{1 + \dfrac{1}{Q_p^2}} - \dfrac{1}{Q_p}) \\ \tau_\epsilon^p = \dfrac{1}{\omega^2\tau_\sigma} \\ \tau_\epsilon^s = \dfrac{1 + \omega\tau_\sigma Q_s}{\omega Q_s - \omega^2\tau_\sigma}. \end{cases} \tag{2}$$

We use a simple gridding scheme to represent the $x-z$ borehole plane. The plane is partitioned into a near-field region, with fine spacing to resolve borehole phenomena, a far-field, with a large grid spacing constrained by numerical dispersion, and a transition region where the grid spacing smoothly varies between these extremes (see figure 1). This approach avoids the spurious reflection problems associated with sudden changes in grid spacing. Similar techniques have recently been explored for surface geometries using both FD (Pitarka, 1999) and pseudo-spectral (Nielsen et al., 1994) methods.

Solving the viscoelastic wave equation on a non-uniform grid requires the spatial derivatives in equation (1) to be approximated using a stretched stencil. Several techniques exist for effectively calculating the coefficients for the stretched difference operators: we use the method of undetermined coefficients (Pitarka, 1999) to pre-compute explicit 4th order operators for all spatial locations. Since the mesh is only distorted along the x and z axis, coefficients are invariant along grid lines, reducing the memory required for stencil storage. The non-uniform mesh is also staggered to increase stability and minimize numerical dispersion: a staggered scheme is crucial for handling the solid-liquid contact present within the borehole. Time derivatives are staggered across the velocity and stress variables and are approximated using an explicit second order central difference operator.

Spatial discretization (h) and temporal increments Δt are chosen to minimize dispersion and maintain stability during the computation. In particular, the inequalities

$$h_{max} < \frac{V_{min}}{5\, f_{max}} \tag{3}$$

$$\Delta t < \frac{0.495\, h_{min}}{V_{max}}, \tag{4}$$

are enforced, where h_{max} and h_{min} are minimum and maximum grid spacings; f_{max} is the maximum frequency of the propagating signal, and V_{min} and V_{max} are the lowest and highest phase velocity respectively. The two phase velocities can be expressed as

$$V_{min} = min(\sqrt{\tau_\epsilon^p/\tau_\sigma}V_p, \sqrt{\tau_\epsilon^s/\tau_\sigma}V_s) \tag{5}$$

$$V_{max} = max(\sqrt{\tau_\epsilon^p/\tau_\sigma}V_p). \tag{6}$$

To minimize artificial boundary reflections, sponge absorbing boundary conditions (Cerjan et al., 1985) are used at the edges of the model. The absorbing sponge is created by including tapered 20-point buffer region of low Q material.

Examples

To demonstrate the benefits of incorporating a variable mesh for single-well models, we now present a pair of numerical examples. The first example, composed only of a vertical well and a simple sediment-salt interface, is used to explore the wide range of wave phenomenon captured by our viscoelastic modeling code. The second test model incorporates a realistic geological structure more typical of the salt-flank plays where single-well imaging is currently being applied. The results from both seismic simulations show reflections from the primary targets which are partially obscured by strong borehole modes over limited temporal windows.

In the first model the borehole is uncased, 14cm in diameter, and water filled. The source function used to excite the model is a Ricker wavelet with a central frequency of 500Hz. Figure (1) shows the computational mesh used in the vicinity of the borehole. The lateral grid spacing

Downloaded 01 Dec 2011 to 171.64.173.107. Redistribution subject to SEG license or copyright; see Terms of Use at http://segdl.org/

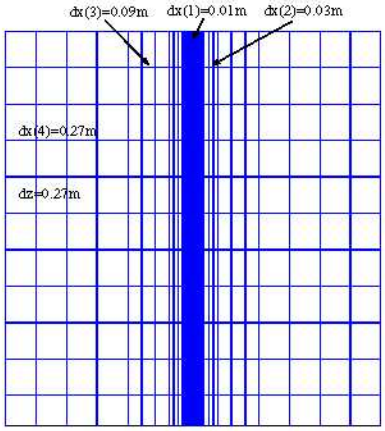

Fig. 1: Grid spacing at the vicinity of the borehole. The horizontal grid spacing smoothly increases from 0.01m to 0.27m over 0.36m wide transition region. The vertical grid spacing is 0.27m throughout the grid.

smoothly increases from 0.01m to 0.27m over a transition region 0.36m wide. The vertical spacing is 0.27m throughout the grid.

The property contrast between the salt ($V_p = 4550$ m/s, $V_s = 2630$ m/s, $\rho = 2160\ kg/m^3$, $Q_p = 200$, $Q_s = 100$) and the surrounding sediments ($V_p = 2500$ m/s, $V_s = 1527$ m/s, $\rho = 2050\ kg/m^3$, $Q_p = 55$, $Q_s = 30$) produces high amplitude reflections. A snapshot of the τ_{zz} component of the wavefield recorded at 21 ms, figure 2, shows a multitude of active modes. In addition to direct waves (P, S) and a strong tube wave (T), salt flank reflections (PPr, PSr, SPr) and transmitted waves (PPt, PSt, SSt) are visible.

Our second model (Figure 3) incorporates a more complex geological structure, including several dipping sediment layers and a pair of salt-bounded petroleum traps. The borehole parameters used are identical to those described in the first example but the central frequency of the source wavelet is 250 Hz. Table 1 provides the physical properties of the model layers. Note that model components 7 and 8 are oil-saturated sections of layers 5 and 3 respectively, while component 9 is a gas pocket in layer 2.

A pressure seismogram and the τ_{zz} component snapshot of the wavefield are shown in figures 4 and 5. This example reveals both the high level of wavefield complexity introduced by a small number of lithological boundaries and the effectiveness of our variable grid FD code in handling multiple-scale models.

Conclusions

In this paper, we have discussed an efficient variable grid finite-difference algorithm, suitable for solving the viscoelastic wave equation in 2D. Use of a non-uniform mesh enables us to include a properly scaled borehole within a larger computational domain. The resulting code has been applied to two single-well models, yielding

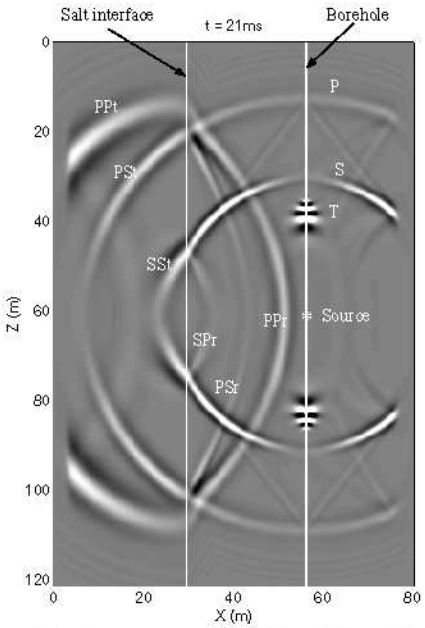

Fig. 2: Snapshot of τ_{zz} component. P, S, and T are direct P-wave, S-wave and tube wave; PPr is the P reflection; PSr and SPr are P-to-S, and S-to-P converted reflections; PPt and SSt are the P and S transmissions, respectively; PSt is P-to-S converted transmission.

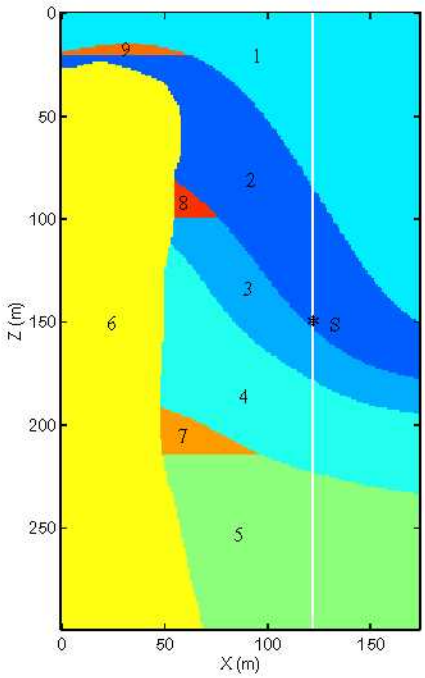

Fig. 3: Realistic salt flank model

Downloaded 01 Dec 2011 to 171.64.173.107. Redistribution subject to SEG license or copyright; see Terms of Use at http://segdl.org/

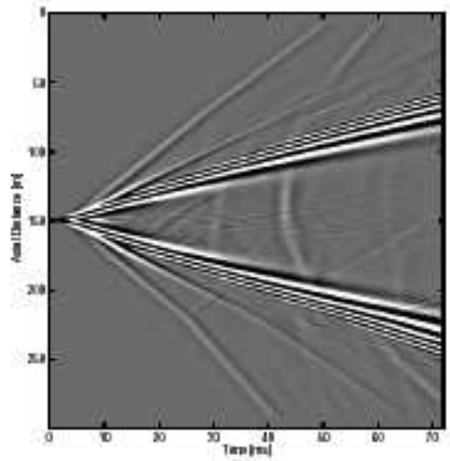

Fig. 4: Synthetic seismogram of pressure in the borehole.

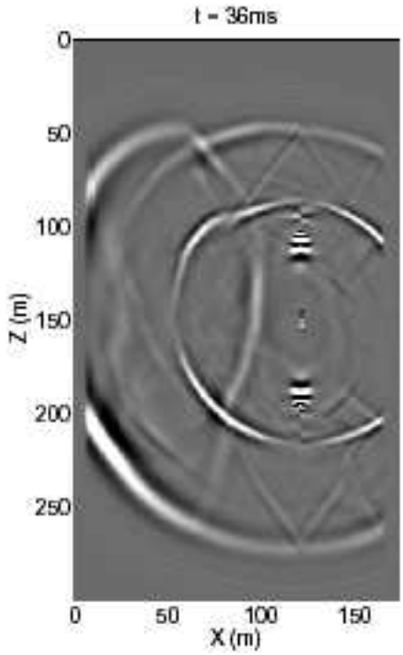

Downloaded 01 Dec 2011 to 171.64.173.107. Redistribution subject to SEG license or copyright; see Terms of Use at http://segdl.org/